BMC Research Notes

RESEARCH NOTE

Open Access

Morphological study of embryonic *Chd8*$^{+/-}$ mouse brains using light-sheet microscopy

Harold F. Gómez[1,2†], Leonie Hodel[1†], Odyssé Michos[1,2] and Dagmar Iber[1,2*]

Abstract

Objective: Autism spectrum disorder (ASD) encompasses a group of neurodevelopmental conditions that remain poorly understood due to their genetic complexity. *CHD8* is a risk allele strongly associated with ASD, and heterozygous *Chd8* loss-of-function mice have been reported to exhibit macrocephaly in early postnatal stages. In this work, we sought to identify measurable brain alterations in early embryonic development.

Results: We performed light-sheet fluorescence microscopy imaging of N-cadherin stained and optically cleared *Chd8*$^{+/-}$ and wild-type mouse brains at embryonic day 12.5 (E12.5). We report a detailed morphometric characterization of embryonic brain shapes and cortical neuroepithelial apical architecture. While *Chd8*$^{+/-}$ characteristic expansion of the forebrain and midbrain was not observed this early in embryogenesis, a tendency for a decreased lateral ventricular sphericity and an increased intraocular distance in *Chd8*$^{+/-}$ brains was found compared to controls. This study advocates the use of high-resolution microscopy technologies and multi-scale morphometric analyses of target brain regions to explore the etiology and cellular basis of *Chd8* haploinsufficiency.

Keywords: Light-sheet microscopy, Chd8, Mouse brains, Autism, Tissue clearing, Morphometry, Lewis' law, Aboav-weaire's law

Introduction

Autism spectrum disorder (ASD) is a poorly understood disease due to significant genetic complexity and phenotypic heterogeneity. Despite our improved understanding of how ASD develops [1–5], mapping the relative contribution of risk alleles to neuroanatomical abnormalities and clinically observed phenotypes like macrocephaly remains challenging.

Genetic studies have implicated mutations in more than 800 genes in the etiology of ASD [1]. One of the most strongly associated genes is the chromodomain helicase DNA-binding protein 8 *CHD8*, an ATP-dependent chromatin remodeler, and transcriptional repressor. Patients with loss-of-function (LOF) mutations in *CHD8* exhibit gene haploinsufficiency, display altered behavior, and region-specific anomalies in brain morphology and physiology that manifest during early childhood [6–8]. Similarly, *Chd8* haploinsufficiency in mice results in neonatal macrocephaly, increased brain weight, and craniofacial abnormalities [9–11], mirroring clinical observations in patients and suggesting similar developmental trajectories between species.

ASDs are largely hypothesized to originate in utero from profound perturbations in neural stem cell niche regions of the developing brain [12]. Gene expression profiling in the embryonic mouse cortex of *Chd8* haploinsufficient mice shows a temporal modulation of *Chd8* that peaks at E12, and helps negotiate the balance between neuronal expansion (prior to E12.5) and differentiation (E12.5 to postnatal) [13]. Consequently, dysregulations of *Chd8* dynamics during cortical development in mice prematurely deplete the neural progenitor pool, consistent with the lower density of neural cells

*Correspondence: dagmar.iber@bsse.ethz.ch
†Harold F. Gómez and Leonie Hodel contributed equally to this work
[1] Department of Biosystems, Science and Engineering (D-BSSE), ETH Zurich, Mattenstraße 26, 4058 Basel, Switzerland
Full list of author information is available at the end of the article

and metabolic components observed in children with ASD [14]. Despite novel evidence, it is unknown whether in utero perturbations manifest as distinctive anatomical dysmorphologies before the postnatal onset of characteristic ASD phenotypes [15].

In this study, we investigated the embryonic morphological consequences of *Chd8* haploinsufficiency at the whole-organ and cellular level. To anticipate anatomical findings in a condition with early-life onset, we leveraged N-cadherin stainings, light-sheet microscopy, and tissue clearing to examine the neuroanatomical differences between E12.5 mouse brains with germline *Chd8*$^{+/-}$ LOF mutations [10] and litter-matched wild types. We report slight differences in intraocular distance and ventricular sphericity and introduce a detailed approach for comparing cortical neuroepithelial apical architecture. Taken together, this work provides a new avenue for querying the developmental role of *CHD8* and the cellular remodeling that is likely to precede associated post-birth brain malformations in haploinsufficiency cases.

Main text

Methods and materials

Animals

Mice with *Chd8* LOF mutations were generated using Cas9-mediated germline editing [10]. 2 wild-types and 5 *Chd8*$^{+/-}$ E12.5 mouse brains were used. Mice were kept in individually vented cages with ad libitum food and water in a separate rack. Harem breeding was set up with a single stud male and up to three females. Adults animals were anesthetized with Avertin (375 mg/kg body weight) prior to cervical dislocation.

No inclusion or exclusion criteria were set, and no research protocol was registered prior to analysis. As randomization was not employed, confounders such as the order of treatment measurements or animal/cage locations were not controlled. No humane endpoints were established.

Immunofluorescence on embryonic brains

Specimens were fixed with 4% paraformaldehyde in PBS and incubated with anti-N-cadherin antibody (BD Transduction Laboratories; Material No. 610920; 1:200) at 4 °C for 3 days. After washing in D-PBS, brains were incubated with conjugated fluorescent secondary Alexa Fluor 555 donkey anti-mouse IgG (H + L) (Abcam; Material No. ab150106; 1:250) for 2 days at 4 °C.

Optical clearing and light-sheet imaging

Clearing was performed using the Clear Unobstructed Brain/Body Imaging Cocktails and Computational Analysis (CUBIC) protocol [16]. Reagent-1 [25% (w/w) urea, 25% ethylenediamine, 15% (w/w) Triton X-100 in distilled water] and reagent-2 [25% (w/w) urea, 50% (w/w) sucrose, 10% (w/w) nitrilotriethanol in distilled water] were used. Samples were incubated in 1/2 reagent-1 (CUBIC-1:H_2O = 1:1) for 1 day and then in 1× reagent-1 until transparent. Following several washes in PBS, samples were treated with 1/2 reagent-2 (CUBIC-2:PBS = 1:1) for around 3 days. Incubation in 1× reagent-2 was done until transparent. All steps were performed on a shaker at room temperature. Serial dilutions mitigated tissue expansion [16], and all samples were processed, cleared, and imaged in parallel to minimize downstream systematic errors.

Fluorescence images were acquired using a Zeiss Lightsheet Z.1 microscope. Acquisition optics included a Zeiss 20×/1.0 Plan Apochromat and a Zeiss 5×/0.1 objective lens. Image stacks were deconvolved in Huygens deconvolution and pre-processed using Fiji [17].

3D surface reconstruction of whole mouse brains

The 3D segmentation of the ventricles and cerebral cortex was conducted with Imaris MeasurementPro, a component of Imaris v9.1.2 (BitPlane, South Windsor, CT, USA). Imaris enabled the computational interpolation of planar 2D surface outlines from horizontal sections into 3D iso-surfaces that faithfully delineated small-scale features (Fig. 1). Quantified brain surface features included volume and surface area. Intraocular distance was measured in 3D using measurement points placed in the center of the pupils.

As the cortex has broad irregular anatomical features that make absolute cortical thickness measurements challenging, we considered the cortex to be a hollow cylinder with volume V and area A. In this way, the cortical height of the neuroepithelial layer was approximated as

$$h_{cortex} = \frac{2V_{cortex}}{A_{outer} + A_{inner}}$$

Furthermore, to derive ventricular sphericity, lateral ventricle iso-surfaces were separated at the septum pellucidum. The sphericity of each 3D entity was determined as

$$S_{ventr} = \frac{\pi^{\frac{1}{3}}(6V_{ventr})^{\frac{2}{3}}}{A_{ventr}}$$

Morphometric measurements of apical neuroepithelia

Cell morphology in the apical layer of the cortical epidermis was investigated using MorphoGraphX [18]. A curved 2.5D image projection was constructed by meshing the apical boundary and projecting 2–6 µm of the most apical signal onto it. Then, cell boundaries were semi-automatically segmented, excluding border cells.

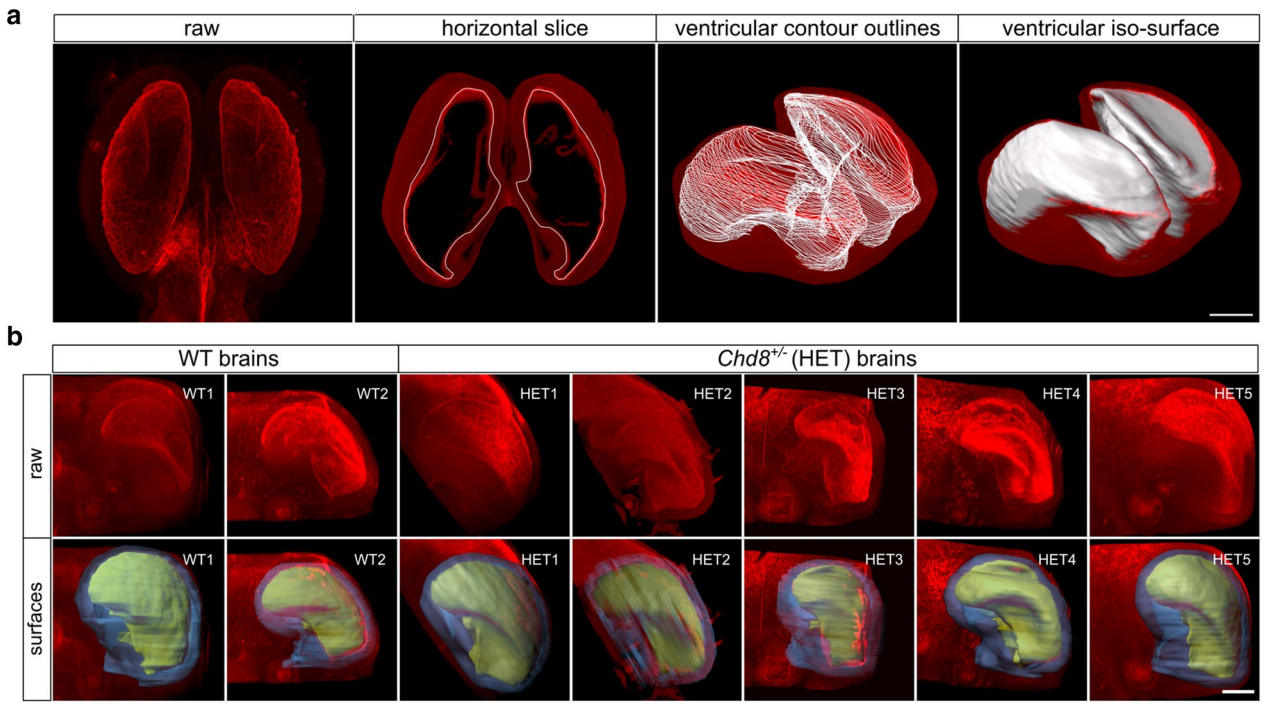

Fig. 1 Volumetric analysis of CUBIC-cleared wild-type and *Chd8*$^{+/-}$ samples, immunostained for N-cadherin (red) to mark neuronal epithelial tissue. **a** Illustration of the processing steps in the creation of manual surfaces. Sequential ventricular contours were drawn manually throughout the entire dataset to extract 3D morphology (white outlines). Scale bar 500 µm. **b** Raw (top row) and overlays (bottom row) of ventricular (yellow) and cortical (blue) iso-surfaces for each sample. Scale bar 400 µm

To characterize the projected polygonal apical lattices, quantifications of cellular areas and neighbour numbers were imported into the R software platform. Apical packing was explored via known regularities of epithelial lattices. Termed Lewis' Law, this property linearly relates the measured average cell area A and neighbour number n and has been previously described in all apical epithelia studied to date [19, 20].

$$\frac{\bar{A}_n}{\bar{A}} = \frac{(n-2)}{4}$$

As cells with small polygon numbers have the tendency to be in contact with cells of larger polygon numbers and vice-versa, one also observes that the average number of neighbours of all n cells that border a cell with n neighbours follows

$$m(n) = 5 - \frac{n}{8}$$

a relationship termed Aboav-Weaire's Law [21, 22]. Lastly, the cell aspect ratio was calculated using an in-house algorithm that leverages MorphoGraphX's modularity to fit an ellipse and extract major and minor axes for each cell outline.

Results

ASD-associated craniofacial phenotypes in Chd8$^{+/-}$ *mice*

To determine whether *Chd8*$^{+/-}$ mice exhibit structural and craniofacial ASD phenotypes during embryonic development, we tested for morphological differences. To this extent, 3D segmentation was used to derive iso-surface representations from volumetric image stacks and enable the quantification of size, shape, and asymmetry (Fig. 1).

We then characterized different anatomical features in cortical and ventricular regions to reveal regional alterations (Fig. 2). Overall brain volume, including ventricles, showed no significant difference between the two groups (wild-type [n = 2] 3.41 mm^3 and 3.15 mm^3, *Chd8*$^{+/-}$ [n = 5] 3.60 ± 0.56 mm^3) (Fig. 2a). Similarly, measured cortical volumes excluding the ventricular space showed no difference (wild-type [n = 2] 2.17 mm^3 and 2.15 mm^3, *Chd8*$^{+/-}$ [n = 5]: 2.47 ± 0.37 mm^3). Individual ventricular volume was consistent within and between groups (wild-type [n = 4] 0.56 ± 0.07 mm^3, *Chd8*$^{+/-}$ [n = 10] 0.57 ± 0.14 mm^3). Furthermore, we observed no differences in brain surface area (wild-type [n = 2] 15.6 mm^2 and 14.5 mm^2, *Chd8*$^{+/-}$ [n = 5] 15.48 ± 1.63 mm^2) or in ventricular surface area (wild-type [n = 4] 4.66 ± 0.30 mm^2, *Chd8*$^{+/-}$ [n = 10]

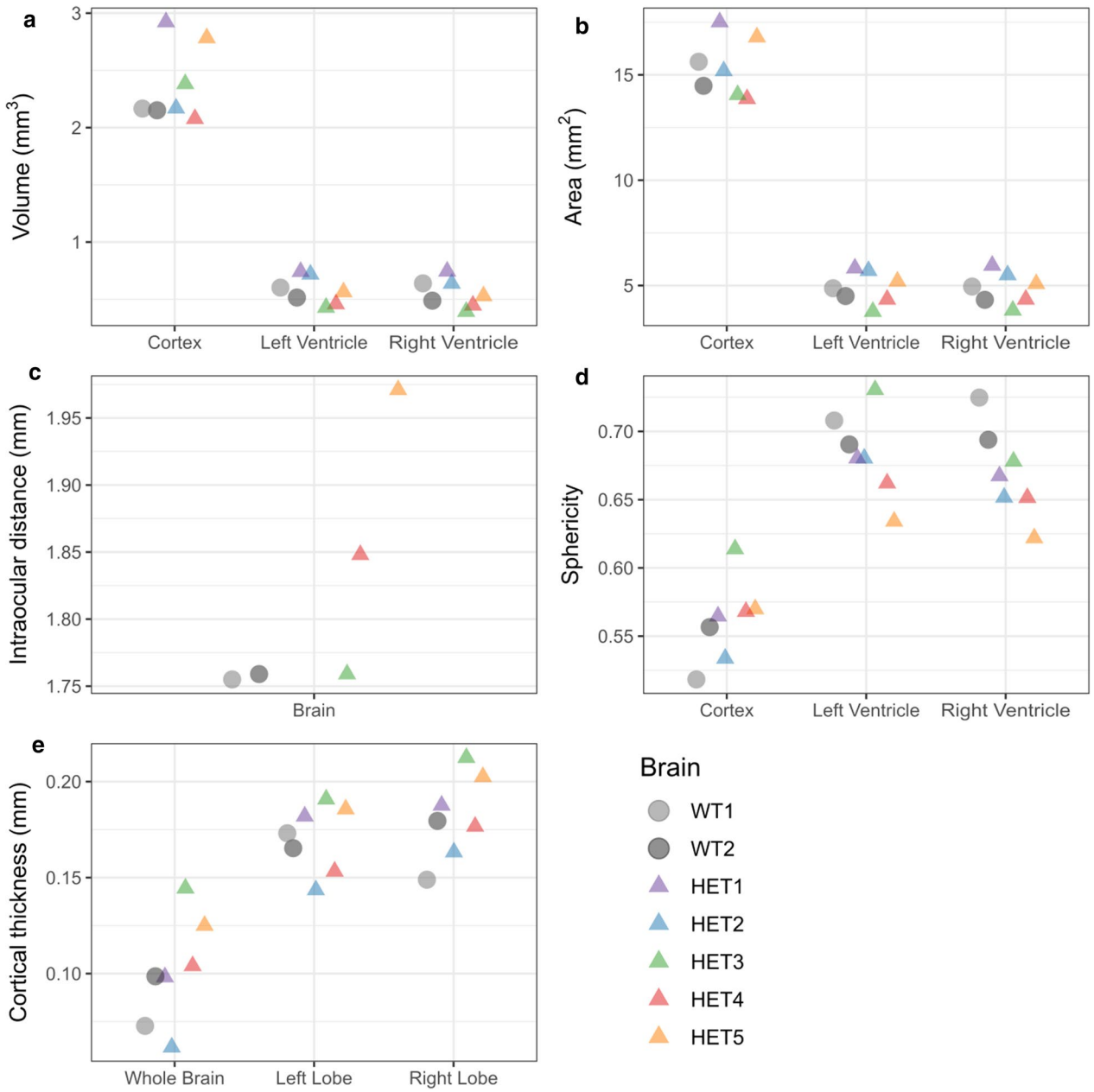

Fig. 2 Morphological characterization of E12.5 wild-type and *Chd8*$^{+/-}$ mouse brains. **a**–**c** Cortical and ventricular **a** volume, **b** surface area, and **c** intraocular distance. **d** Sphericity of cortex and ventricles. **e** Cortical thickness of whole brains and left and right lobes. Quantifications were extracted from ventricular and cortical iso-surfaces

4.95 ± 0.83 mm^2) between *Chd8*$^{+/-}$ and wild types (Fig. 2b).

CHD8 mutant patients often present craniofacial abnormalities [7]. We report a slight increase in the intraocular distance and variability within the *Chd8*$^{+/-}$ group (wild-type [n = 2] 1.75 ± 0.002 mm, *Chd8*$^{+/-}$ [n = 3] 1.85 ± 0.10 mm) (Fig. 2c), which is consistent with mouse studies from similar genetic backgrounds [10]. Moreover, we observed a slight decrease in ventricular sphericity in *Chd8*$^{+/-}$ mice (wild-type [n = 4] 0.70 ± 0.01, *Chd8*$^{+/-}$ [n = 10] 0.67 ± 0.03) (Fig. 2d). We also found a higher variability in whole-brain cortical thickness in *Chd8*$^{+/-}$ mice (wild-type [n = 2] 0.08 ± 0.02 mm, *Chd8*$^{+/-}$ [n = 5] 0.10 ± 0.03 mm) (Fig. 2e). Thus, only some craniofacial phenotypes were detected during early embryonic development.

Quantifying apical cell morphology in Chd8$^{+/-}$ mice

To identify cellular and tissue mechanics abnormalities, we isolated and meshed the apical boundaries of cell patches in matching regions of the cerebral cortex [18]. By taking tissue curvature into account, we segmented a large number of cell outlines from one *Chd8*$^{+/-}$ [n = 3854] and one wild-type [n = 1031] sample (Fig. 3a, b).

Apical organization was quantified by geometrical properties like cell number of neighbours, areas, and aspect ratio. We found similar hexagon and heptagon frequencies (wild-type 29% hexagons, 16% heptagons, *Chd8*$^{+/-}$ 31% hexagons, 20% heptagons) (Fig. 3c). The observed relation between the polygon type of cells *n* and the average polygon type of their neighbours m_n termed Aboav-Weaire's Law [21, 22], recapitulated results in both the *Drosophila* wing disc and chicken neural tube epithelium [23] (Fig. 3d). Similarly, we compared area distributions per polygon type and found no significant difference. The average area per polygon type followed a linear dependency in both samples; a relationship termed Lewis' Law [19, 20] (Fig. 3e). Moreover, considering local apical curvature, the aspect ratio was determined by fitting an ellipse to each cell outline and extracting the major and minor axes. The aspect ratio distribution of the *Chd8*$^{+/-}$ cells was minimally wider than in the wild type (Fig. 3f).

Discussion

Chd8 haploinsufficient mice display ASD-like phenotypes that parallel the clinical signature of individuals with de-novo *CHD8* mutations [10, 11, 13, 24]. Consistent with retrospective patient head circumference data, mouse models suggest a postnatal onset of abnormal head growth [10, 11]. In this study, we queried the neuroanatomy of E12.5 *Chd8*$^{+/-}$ and litter-matched controls using light-sheet microscopy to determine whether anomalies in brain and cortical cell shape preindicate ASD-associated macrocephaly. As there are no reported alterations in macroscopic or cellular structures beyond a small degree of swelling in optically cleared brains [25], we also leveraged CUBIC dilutions to permit the 3D staining and imaging of morphological features and cellular architectures.

Longitudinal studies of postnatal volumetric brain changes have implicated neuroanatomical abnormalities in cortical thickness, ventricular morphology, cortical overgrowth, and increased cortical surface area in the developmental trajectory of ASDs [6, 26–31]. Accordingly, our work characterized cortical thickness and volumetric features to confirm whether analogous alterations are observable in haploinsufficient mice. We note that no significant discrepancies in cortical thickness, ventricular and cortical volumes or surface areas between groups could be determined. In line with the heterogeneous nature of ASD, it is reasonable to assume that other brain regions may be affected instead. Notably, we provide experimental evidence of dissimilarities in ventricular sphericity and intraocular distance that mirror known phenotypes in haploinsufficient adult mice (Fig. 2) [10].

Similarly, aberrations at the cellular scale have been reported during the establishment of cortical microarchitecture in ASD [27]. Consequently, we sought to ascertain differences in the cortical organization as defined by patterns of cell geometric features on the apical surface (Fig. 3). Having quantified epithelial morphology according to the cell area, aspect ratio, neighbour topology, and adherence to empirical laws such as Lewis' and Aboav-Weaire's (Fig. 3), our data showed no departure in the cortical organization between groups, suggesting similar mechanical behaviour [20, 22].

In this work, we present a multi-scale assessment of the embryonic neuroanatomical implications of *Chd8* haploinsufficiency in mice. We propose that an increased understanding of the identified organ-level differences may shed light on the etiology of hypertrophic brain growth. What is more, our approach opens exciting avenues to investigate cellular alterations in other implicated brain regions and phenotypic differences across diverse *Chd8* haploinsufficient mouse models, all of which have a wide range of dosage-specific, dimorphic, and behavioural signatures [24, 32].

Limitations

Underscoring the complexity of autism, our results did not show statistically significant differences in overall morphology except for slight deviations in ventricular sphericity and intraocular distance (Fig. 2). Furthermore, we did not identify aberrations in cortical cellular

(See figure on next page.)

Fig. 3 Quantification of apical cell morphology in wild-type [n = 1031] and *Chd8*$^{+/-}$ [n = 3854] E12.5 mouse brains. **a**, **b** 2.5D segmentation overlay of the apical surface of **a** *Chd8*$^{+/-}$ (HET) and **b** wild-type (WT) neurocortical epithelium. Scale bar: 20 µm. **c** Distribution of apical neighbour numbers per sample. The average number of cell neighbours is 5.84 for WT and 5.80 for HET, which is close to the topological requirement of 6. **d** Polygon type *n* times the mean polygon number of neighbours *m* of the cell *n* follows a linear relationship termed Aboave-Weaire's Law. **e** Average apical cell area by cell neighbour number following a linear relationship termed Lewis' Law (black line). **f** Cellular aspect ratios between their longest and shortest axis

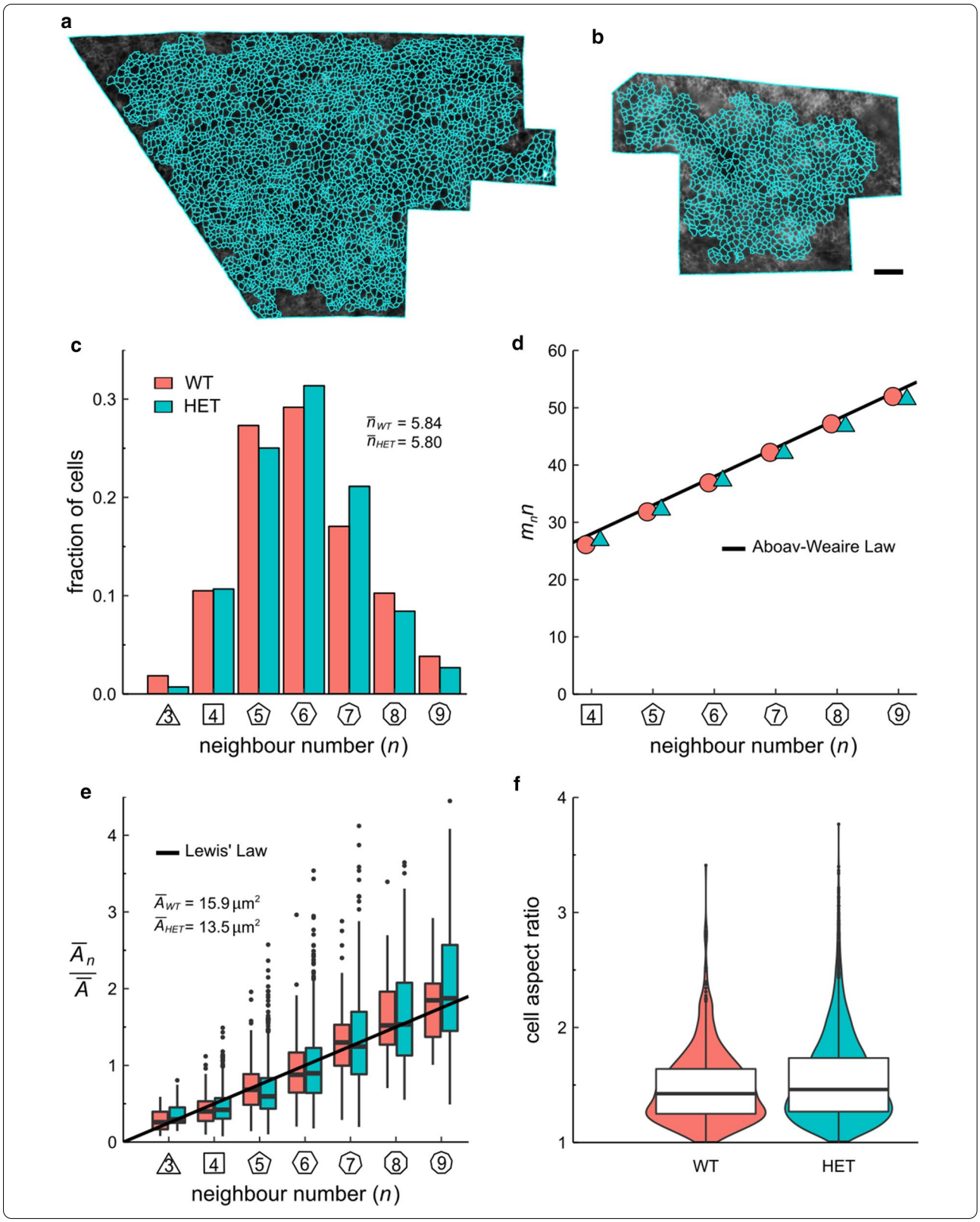
a
b
c
WT
HET
$\overline{n}_{WT}$ = 5.84
$\overline{n}_{HET}$ = 5.80
fraction of cells
neighbour number (n)
d
$m_n n$
Aboav-Weaire Law
neighbour number (n)
e
Lewis' Law
$\overline{A}_{WT}$ = 15.9 µm²
$\overline{A}_{HET}$ = 13.5 µm²
$\frac{\overline{A}_n}{\overline{A}}$
neighbour number (n)
f
cell aspect ratio
WT
HET

architecture (Fig. 3). We acknowledge that as only a small sample size could be studied (wild-type [n = 2], and *Chd8*$^{+/-}$ [n = 5]), small morphological differences may have been missed due to the lack of statistical power.

Abbreviations
ASD: Autism spectrum disorder; CHD8: Chromodomain helicase DNA-binding protein 8; LOF: Loss-of-function; CUBIC: Clear unobstructed brain/body imaging cocktails and computational analysis; WT: Wild type; HET: Heterozygous.

Acknowledgements
We would like to thank Randall Platt and Ashwin S. Shetty for providing the embryos. Moreover, we acknowledge Richard S. Smith for his expert advice on extending MorphoGraphX to enable aspect ratio quantifications of segmented cell outlines.

Authors' contributions
The study was designed by DI. OM, HG generated the data, HG, LH analyzed the data and wrote the manuscript. All authors read and approved the final manuscript.

Funding
This work has been supported through an SNF Sinergia grant to DI.

Availability of data and materials
The datasets used and/or analyzed during the current study are available from the corresponding author on reasonable request.

Ethics approval and consent to participate
All animal experiments conducted in the USA followed Public Health Service (PHS) policy and guidelines on humane care, and the use of laboratory animals was approved by the Massachusetts Institute of Technology Committee for Animal Care (CAC).

Consent for publication
Not applicable.

Competing interests
The authors declare that the research was conducted in the absence of any commercial or financial relationships that could be construed as a potential conflict of interest.

Author details
[1] Department of Biosystems, Science and Engineering (D-BSSE), ETH Zurich, Mattenstraße 26, 4058 Basel, Switzerland. [2] Swiss Institute of Bioinformatics (SIB), Mattenstraße 26, 4058 Basel, Switzerland.

Received: 5 October 2020 Accepted: 28 December 2020
Published online: 12 January 2021

References

1. Abrahams BS, Geschwind DH. Advances in autism genetics: on the threshold of a new neurobiology. Nat Rev Genet. 2008;9(5):341–55.
2. Iossifov I, Ronemus M, Levy D, Wang Z, Hakker I, Rosenbaum J, et al. De novo gene disruptions in children on the autistic spectrum. Neuron. 2012;74(2):285–99.
3. O'Roak BJ, Deriziotis P, Lee C, Vives L, Schwartz JJ, Girirajan S, et al. Exome sequencing in sporadic autism spectrum disorders identifies severe *de novo* mutations. Nat Genet. 2011;43(6):585–9.
4. Parikshak NN, Luo R, Zhang A, Won H, Lowe JK, Chandran V, et al. Integrative functional genomic analyses implicate specific molecular pathways and circuits in autism. Cell. 2013;155(5):1008–21.
5. Sanders SJ, Murtha MT, Gupta AR, Murdoch JD, Raubeson MJ, Willsey AJ, et al. De novo mutations revealed by whole-exome sequencing are strongly associated with autism. Nature. 2012;485(7397):237–41.
6. Courchesne E. Evidence of brain overgrowth in the first year of life in autism. JAMA. 2003;290(3):337.
7. Bernier R, Golzio C, Xiong B, Stessman HA, Coe BP, Penn O, et al. Disruptive CHD8 mutations define a subtype of autism early in development. Cell. 2014;158(2):263–76.
8. Xu Q, Liu Y, Wang X, Tan G, Li H, Hulbert SW, et al. Autism-associated CHD8 deficiency impairs axon development and migration of cortical neurons. Mol Autism. 2018;9(1):65.
9. Sugathan A, Biagioli M, Golzio C, Erdin S, Blumenthal I, Manavalan P, et al. CHD8 regulates neurodevelopmental pathways associated with autism spectrum disorder in neural progenitors. Proc Natl Acad Sci. 2014;111(42):E4468–77.
10. Platt RJ, Zhou Y, Slaymaker IM, Shetty AS, Weisbach NR, Kim J-A, et al. Chd8 mutation leads to autistic-like behaviors and impaired striatal circuits. Cell Rep. 2017;19(2):335–50.
11. Katayama Y, Nishiyama M, Shoji H, Ohkawa Y, Kawamura A, Sato T, et al. CHD8 haploinsufficiency results in autistic-like phenotypes in mice. Nature. 2016;537(7622):675–9.
12. Corley MJ, Vargas-Maya N, Pang APS, Lum-Jones A, Li D, Khadka V, et al. Epigenetic delay in the neurodevelopmental trajectory of DNA methylation states in autism spectrum disorders. Front Genet. 2019;10:907.
13. Durak O, Gao F, Kaeser-Woo YJ, Rueda R, Martorell AJ, Nott A, et al. Chd8 mediates cortical neurogenesis via transcriptional regulation of cell cycle and Wnt signaling. Nat Neurosci. 2016;19(11):1477–88.
14. Dager SR, Friedman SD, Petropoulos H, Shaw DWW. Imaging evidence for pathological brain development in autism spectrum disorders. Totowa: Humana Press; 2008. p. 361–79.
15. Fein D. The neuropsychology of autism. OUP USA; 2011. 559 p.
16. Susaki EA, Tainaka K, Perrin D, Yukinaga H, Kuno A, Ueda HR. Advanced CUBIC protocols for whole-brain and whole-body clearing and imaging. Nat Protoc. 2015;10(11):1709–27.
17. Schindelin J, Arganda-Carreras I, Frise E, Kaynig V, Longair M, Pietzsch T, et al. Fiji: an open-source platform for biological-image analysis. Nat Methods. 2012;9(7):676–82.
18. Barbier de Reuille P, Routier-Kierzkowska A-L, Kierzkowski D, Bassel GW, Schüpbach T, Tauriello G, et al. MorphoGraphX: a platform for quantifying morphogenesis in 4D. eLife. 2015;4:e05864.
19. Lewis FT. The correlation between cell division and the shapes and sizes of prismatic cells in the epidermis of cucumis. Anat Rec. 1928;38(3):341–76.
20. Kokic M, Iannini A, Villa-Fombuena G, Casares F, Iber D. Minimisation of surface energy drives apical epithelial organisation and gives rise to Lewis' law. Biophysics. 2019.
21. Aboav D. The arrangement of grains in a polycrystal. Metallography. 1970;3(4):383–90.
22. Vetter R, Kokic M, Gómez H, Hodel L, Gjeta B, Iannini A, et al. Aboave-Weaire's law in epithelia results from an angle constraint in contiguous polygonal lattices. Biophysics. 2019.
23. Sánchez-Gutiérrez D, Tozluoglu M, Barry JD, Pascual A, Mao Y, Escudero LM. Fundamental physical cellular constraints drive self-organization of tissues. EMBO J. 2016;35(1):77–88.
24. Gompers AL, Su-Feher L, Ellegood J, Copping NA, Riyadh MA, Stradleigh TW, et al. Germline Chd8 haploinsufficiency alters brain development in mouse. Nat Neurosci. 2017;20(8):1062–73.
25. Tainaka K, Kubota SI, Suyama TQ, Susaki EA, Perrin D, Ukai-Tadenuma M, et al. Whole-body imaging with single-cell resolution by tissue decolorization. Cell. 2014;159(4):911–24.
26. Courchesne E, Pierce K, Schumann CM, Redcay E, Buckwalter JA, Kennedy DP, et al. Mapping early brain development in autism. Neuron. 2007;56(2):399–413.
27. Donovan APA, Basson MA. The neuroanatomy of autism—a developmental perspective. J Anat. 2017;230(1):4–15.
28. Bigler ED, Tate DF, Neeley ES, Wolfson LJ, Miller MJ, Rice SA, et al. Temporal lobe, autism, and macrocephaly. Am J Neuroradiol. 2003;24(10):2066–76.
29. Herbert MR, Ziegler DA, Deutsch CK, O'Brien LM, Lange N, Bakardjiev A, et al. Dissociations of cerebral cortex, subcortical and cerebral white matter volumes in autistic boys. Brain. 2003;126(5):1182–92.
30. Hazlett HC, Poe M, Gerig G, Smith RG, Provenzale J, Ross A, et al. Magnetic resonance imaging and head circumference study of brain size in autism: birth through age 2 years. Arch Gen Psychiatry. 2005;62(12):1366.

31. Hazlett HC, Poe MD, Gerig G, Smith RG, Piven J. Cortical gray and white brain tissue volume in adolescents and adults with Autism. Biol Psychiat. 2006;59(1):1–6.
32. Jung H, Park H, Choi Y, Kang H, Lee E, Kweon H, et al. Sexually dimorphic behavior, neuronal activity, and gene expression in Chd8-mutant mice. Nat Neurosci. 2018;21(9):1218–28.

Publisher's Note